



Science Arts & Métiers (SAM)

is an open access repository that collects the work of Arts et Métiers Institute of Technology researchers and makes it freely available over the web where possible.

This is an author-deposited version published in: <https://sam.ensam.eu>
Handle ID: <http://hdl.handle.net/10985/23923>

To cite this version :

Martin BOURHIS, Michaël PEREIRA, Florent RAVELET - Performance and flow characteristics of the optimum rotors of Betz, Joukowsky, and Glauert at low tip-speed ratio - Physics of Fluids - Vol. 34, n°10, p.105105 - 2022

Any correspondence concerning this service should be sent to the repository

Administrator : scienceouverte@ensam.eu



Performance and flow characteristics of the optimum rotors of Betz, Joukowski and Glauert at low tip-speed ratio

M. Bourhis,^{1, a)} M. Pereira,¹ and F. Ravelet¹

Arts et Metiers Institute of Technology, CNAM, LIFSE, HESAM University, 75013 Paris, France

(*Electronic mail: martin.bourhis@ensam.eu)

(Dated: 22 August 2022)

The advent of Internet of Things technology has led to a renewed interest in the use of low tip-speed ratio micro-scale wind turbines to supply power to battery-less microsystems. At low tip-speed ratio (λ), the blade geometry varies significantly depending on the optimal flow conditions used in the classical design method, the Blade Element/Momentum theory (BEMT), and very few papers have examined this controversy. This experimental study aims to investigate the airflow and power characteristics of three 200 cm wind turbines designed according to the BEMT with three different optimum flow conditions at $\lambda = 1$: the Betz model, the Glauert model and the Joukowski model. Glauert optimum rotor achieves higher maximum power coefficient ($C_{p,max} = 0.34$) than the optimum rotors of Betz ($C_{p,max} = 0.31$) and Joukowski ($C_{p,max} = 0.26$). The two latter turbines have lower cut-in wind speed and their torque coefficient decreases linearly with the tip-speed ratio. Betz optimum rotor has a highly stable and persistent wake whereas large recirculation bubbles and vortex breakdown are observed downstream the runners of Glauert and Joukowski. The airflow velocity fields and induction factors distributions computed from Stereoscopic Particle Image Velocimetry acquisitions show significant differences between each rotor and also between the theoretical developments and the experimental results, especially for the Joukowski rotor. In addition, even though the optimum flow conditions of Glauert or Betz appears to be the most appropriate models, a method based on flow deflection rather than on airfoil polar plots may be more pertinent for the design of low tip-speed ratio micro-scale wind turbines.

Keywords: Wind turbine, Low tip-speed ratio, Performance, Stereoscopic Particle Image Velocimetry, Blade Element Momentum Theory

I. INTRODUCTION

The current fast development of Internet of Things (IoT) devices raises the question of their supply in power. By Internet of Things, we mean a network of interconnected physical devices able to collect and share data.¹ For example, IoT appliances can be used to perform real-time environmental monitoring by measuring and transmitting environmental data such as air, water or soil quality through wireless sensors. These systems are supposed to be deployed everywhere and to be accessible any time from anywhere, hence it implies high requirements for energy storage and power management.² Currently, batteries are widely used to power autonomous sensors but their use presents major drawbacks. The finite amount of energy available, the high cost of replacement or the possible difficulties to have access to it in hazardous locations for maintenance limit the spread of these devices. The use of ambient energy sources such as solar energy, thermal energy or mechanical energy could be considered as a solution to reduce or eliminate batteries in IoT endpoints. Wind energy is one of the available renewable resource of energy. Even though wind power is highly intermittent, a recent study carried out by Wen *et al.*³ emphasises that the average wind speed in major Chinese cities is essentially within the range of 1 m.s^{-1} to 7 m.s^{-1} . Consequently, miniature wind energy harvesters, such as micro-scale wind turbines, could collect the energy

of low speed airflow in urban area to power a rechargeable battery or a capacitor.⁴

Large-scale wind turbines play already an essential role in electricity generation in industrialised countries. At large-scale, the most efficient wind machines are fast, three-bladed and low solidity horizontal axis wind turbines. They can convert up to 40 – 50% of the kinetic power of the wind into mechanical power at high tip-speed ratio λ , of the order of 5 to 7^{5-7} where the tip-speed ratio is the ratio of the tip-velocity $R_T \omega$ to the freestream wind velocity V_∞ :

$$\lambda = \frac{R_T \omega}{V_\infty} \quad (1)$$

R_T is the tip radius of the rotor and ω its angular velocity. Their high efficiency has been made possible by the aerodynamic optimisation of the blades through the choice of optimum chord c and pitch angle β distributions (see Fig. 1 for visualisation of c and β), number of blades N , design tip-speed ratio and also thanks to decades of research in airfoil shape. Conventional modern large-scale wind turbines have a low blade solidity, of a few percent, and have twisted blades with different cross-sectional shape along their span. The blade solidity σ is the ratio of the solid surface area of the blades to the total area swept by the blades:

$$\sigma = \frac{Nc}{2\pi r} \quad (2)$$

N is the number of blades, c is the chord length and r is the radial coordinate.

As micro-scale wind turbines are specifically designed to harvest low energy airflow, their geometry differ substantially

^{a)}Corresponding author

Nomenclature

Greek symbols

ρ	Density of the fluid	V_∞	Free stream wind velocity	P	Mechanical power
ω	Angular velocity	N	Number of blades	P_a	Available power
λ	Tip-speed ratio	R_H	Hub radius	C_p	Power coefficient
λ_{opt}	Optimum tip-speed ratio	R_T	Tip radius	C_τ	Torque coefficient
σ	Blade solidity	H	Hub ratio	$C_{p,max}$	Maximum power coefficient
α	Angle of attack	a	Axial induction factor	dC_p	Infinitesimal power coefficient
α_O	Optimum angle of attack	a'	Tangential induction factor	dC_τ	Infinitesimal torque coefficient
α_c	Critical angle <i>i.e.</i> stall angle	c	Chord length	C_d	Drag coefficient
φ	Relative wind angle	r	Radial coordinate	C_l	Lift coefficient
β	Pitch angle	z	Axial coordinate	C_n	Normal force coefficient
τ	Torque	x	Dimensionless radial coordinate	C_t	Tangential force coefficient
$d\tau$	Infinitesimal torque	C_z	Axial velocity	C_F	Resulting force coefficient
		C_θ	Tangential velocity	W	Relative velocity
		U	Rotating velocity	V_0	Cut-in wind speed

from that of larger ones. Due to low wind speed conditions, micro-scale wind turbines require a high torque to overtake the frictional resistance of the mechanical parts contained in the nacelle and start running. As the turbine's shaft mechanical power P is the product of the angular velocity and the torque τ , a lower optimum tip-speed ratio than large-scale turbines appears to be more appropriate to increase the aerodynamic torque. A large number of blades or wide blades would also help to decrease the cut-in wind speed by increasing the total lift force acting on the turbine and therefore the torque.

Even though an optimum blade solidity, design tip-speed ratio and number of blades seems to be found for fast and large-scale three-bladed turbines, it can be observed from the literature that no consensual agreement exists on the number of blades or blade geometry for low tip-speed ratio micro-scale wind turbines. For instance, the 20 mm turbine of Howey *et al.*⁸, designed to operate at $\lambda = 1$, has 12 blades with a constant chord length and a variable pitch angle. Zakaria *et al.*⁹ designed a 26 mm wind turbine with 8 constant chord blades. Various configurations of micro fan-bladed wind turbines were designed and tested by Leung *et al.*¹⁰. They argued that micro-scale turbine's solidity should be higher than 0.5 and that a high number of blades was preferable.

Kishore *et al.*^{11–13} designed three-bladed and low tip-speed ratio 400 mm and 394 mm turbines with different blade geometries. The blades of the 394 mm turbine were of classical design, with linear twist and tapering from root to tip¹² whereas the chord length of the 400 mm turbine was constant throughout the span and non-linearly twisted¹¹. The experimental tests revealed that the non-conventional turbine reaches higher efficiency than the classical turbine.

Mendonca *et al.*¹⁴ performed wind tunnel tests with 20 cm, 15 cm and 10 cm turbines. Various blade chord length, airfoil shape, pitch angle distributions and number of blades were tested. The results suggest that a decrease in the rotor diameter leads to a decrease in the optimum tip-speed ratio and that higher number of blades increases the efficiency at low tip-speed ratio. Moreover, the authors compared two expressions of blade chord length and pitch angle distributions available in the literature and they found experimentally high differences

in the efficiency and optimum tip-speed ratio between the two turbines.

Many other designs can be found in the open literature^{15–21} with very different blade geometries and level of performance. Even though these studies emphasise together that a decrease in the rotor radius requires a decrease in the design tip-speed ratio and an increase in the blade solidity or number of blades, the design of efficient low tip-speed ratio wind turbines remains an open issue and needs further investigation.

The wide disparity in turbine's geometry and efficiency can be attributed to the absence of consensus on the design method at low tip-speed ratio. Indeed, multiple expressions for the blade chord length and pitch angle distributions are available in the literature and many housemade wind turbines are designed without a theoretical approach. Consequently, it is quite complex to identify and to fully understand the beneficial effects induced by a variation in blade solidity or pitch angle and thus to adopt one design method or another. Whereas very few differences are observed in the blade geometry at high tip-speed ratio, major discrepancies appear at low tip-speed ratio (discussed in the § II) and to date, there has been no detailed experimental investigation on the performance and wake characteristics of low tip-speed ratio turbines designed with different procedures.

Consequently, the aim of the present experimental work is to examine and compare the performance and the flow characteristics upstream and downstream three 200 mm micro-scale horizontal axis wind turbines. All three turbines are designed to achieve their maximum power coefficient at $\lambda = 1$. The blades are designed with the same airfoil but the chord length and pitch angle distributions are computed according to three different design methods: the Betz model, the Glauert model and the Joukowski model. These aerodynamic rotor models result in different optimal blade geometries. The general equations and theoretical results for all three models are detailed in the next section (§ II). Wind turbine geometries are depicted and compared in § III. A description of the wind tunnel experimental setup for collection of power characteristics, cut-in wind speeds and airflow velocity distributions by 3D stereoscopic particle image velocimetry (SPIV) technique

is detailed in § IV and the results are discussed in § V.

II. GENERAL EQUATIONS

The conventional method to compute the chord length c and the pitch angle β distributions is based on two independent theories: the general momentum theory and the blade element theory. This method, which can be used either to estimate the performance of an existing turbine or as a design procedure, is the backbone of all standard turbine design softwares such as QBLADE²² and is commonly known as the Blade Element/Momentum theory (BEMT).

Historically, Betz predicted in 1919 that the efficiency of a turbine cannot exceed $16/27 (\approx 59.3\%)$ using simple one-dimensional axial momentum, mass and energy conservation.²³ Thereafter, Glauert in 1926 developed further the momentum theory. He defined a more general framework, called the general momentum theory, to model the aerodynamic interaction between a rotor and a fluid flow by introducing two-dimensional considerations and rotational velocities to the fluid flow.²⁴ Based on the general momentum theory, Joukowsky derived another set of equations by assuming a constant circulation along the rotor blades.²⁵

In the general momentum theory, a streamtube that encloses the turbine is discretized into annular elements of height dr . The infinitesimal torque $d\tau$ applied by the disc of turbine on an annular element is computed by applying the Euler's turbine theorem to an infinitesimal control volume of thickness dr :

$$d\tau = 2\pi r \rho dr C_z r C_\theta \quad (3)$$

where C_z and C_θ are the axial and tangential flow velocities in the rotor plane (Fig. 1) and ρ is the fluid density.

Introducing the axial a and tangential a' induction factors as:

$$a = \frac{C_z - V_\infty}{V_\infty} \quad (4)$$

$$a' = \frac{C_\theta}{2\omega r} \quad (5)$$

we get the following expressions for the axial velocity C_z , azimuthal velocity C_θ and torque $d\tau$:

$$C_z = V_\infty(1 - a) \quad (6)$$

$$C_\theta = 2a'\omega r \quad (7)$$

$$d\tau = 4\pi \rho r^3 V_\infty (1 - a) \omega a' dr \quad (8)$$

The power coefficient C_p and torque coefficient C_τ are dimensionless coefficients conventionally used to characterise wind turbines' efficiency. The torque coefficient is a dimensionless measure of the torque produced by the turbine and the power coefficient establish power conversion rate:

$$C_\tau = \frac{\tau}{0.5\rho\pi R_T^3 V_\infty^2} \quad (9)$$

$$C_p = \frac{P}{P_a} = \frac{\tau\omega}{0.5\rho\pi R_T^2 V_\infty^3} \quad (10)$$

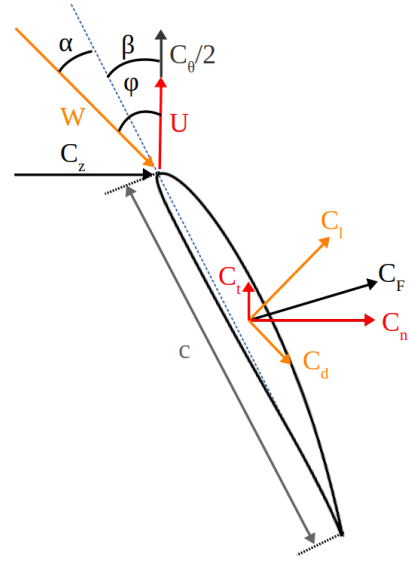


FIG. 1: Velocity triangle on a cross-sectional airfoil element.

They can be obtained from the integration of Eq. 8 from the hub radius R_H to the tip radius R_T of the rotor:

$$C_\tau = \int_{R_H}^{R_T} 8\lambda a'(1 - a)(r/R_T)^3 \frac{dr}{R_T} \quad (11)$$

$$C_p = \int_{R_H}^{R_T} 8\lambda^2 a'(1 - a)(r/R_T)^3 \frac{dr}{R_T} \quad (12)$$

For a given tip-speed ratio λ , Eq. 12 shows that the rotor's maximum efficiency is found by determining the relationship between a and a' for which the power coefficient reaches a maximum value $C_{p,max}$. The resulting conditions on a and a' imply specific induced velocities in the rotor's plane (see Fig. 1). After defining a design tip-speed ratio and optimum flow conditions, an optimum rotor blade geometry can be determined based on the blade element theory. In the current study, we define an optimum rotor as the one designed to achieve $C_{p,max}$. The blade element theory relies on lift and drag polar diagrams of isolated airfoils to compute the blade chord length and pitch angle distributions. The aim of the method is to compute the local loads on many independent blade elements with the help of lift C_l and drag C_d coefficients of a selected airfoil and the optimal induction factors to match with the maximum power coefficient $C_{p,max}$ computed from the general momentum theory (see Refs. 26&27 for theoretical developments). Consequently, the geometry of an optimum rotor is closely linked to the definition of optimum flow conditions.

Betz, Glauert and Joukowsky derived three distinct set of equations for a and a' under different assumptions (see Tab. I). At high tip-speed ratio the optimum spanwise distributions of a and a' derived by the models of Joukowsky, Glauert and Betz follow similar trends (Fig. 2a), especially when the hub ratio $H = R_H/R_T$ is high ($H \geq 0.3$), hence very few changes in the turbine's geometry are noticed by adopting one model or another. It is worth noting that the Glauert's optimum flow

TABLE I: Axial and tangential induction factors equations for each optimum rotor model. $x = r/R_T$ is the spanwise radial coordinate.

	Optimal axial induction factor distribution	Optimal tangential induction factor distribution
Betz	$a = 1/3$	$a' = 0$
Glauert	$16a^3 - 24a^2 + 3a(3 - \lambda^2 x^2) - 1 + \lambda^2 x^2 = 0$	$a' = \frac{1-3a}{4a-1}$
Joukowski	$125a^5 - 325a^4 + 290a^3 - 106a^2 + (17 - 12\lambda^4)a + 4\lambda^2 - 1 = 0$	$a' = \frac{1}{x^2} \frac{3a-1}{5a-1}$

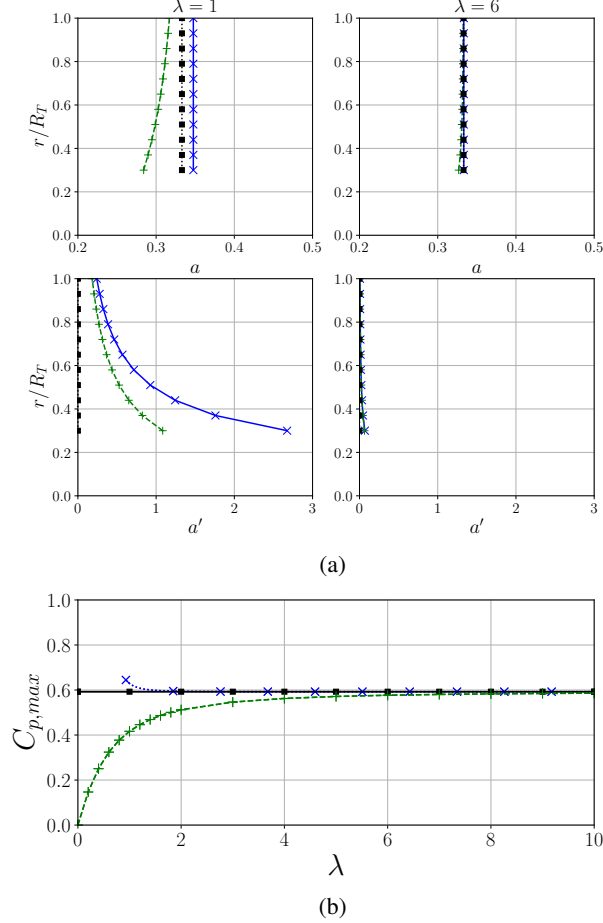


FIG. 2: Comparison of the theoretical optimum flow condition and maximum power coefficient of Betz (■), Glauert (+) and Joukowski (×)(a) Spanwise variations of the optimal induction factors distributions for a tip-speed ratio $\lambda = 1$ (left) and $\lambda = 6$ (right). (b) Variations of the theoretical maximum power coefficient $C_{p,max}$ with the tip-speed ratio λ .

conditions are still the most used equations adopted for the design of turbines and are commonly implemented in design softwares.

However, some controversies exist at low tip-speed ratio. The optimal flow conditions and maximum power co-

efficient $C_{p,max}$ differ substantially when the tip-speed ratio decreases (Fig. 2). For instance, higher power coefficient are predicted at low tip-speed ratio with the model of Joukowski ($C_{p,max}(\lambda = 1) = 0.628$) than the Glauert's model ($C_{p,max}(\lambda = 1) = 0.417$) and the model of Betz ($C_{p,max}(\lambda = 1) = 0.593$). Even though the optimum flow conditions derived by Glauert are mostly used in the design of micro-scale and low tip-speed ratio wind turbines, to date, no experimental data has demonstrated the superiority of one model over another. It partially explains why no consensual agreement exists on the number of blades, pitch angle or blade solidity for micro-scale and low tip-speed ratio wind turbines. Another major theoretical issue and controversial subject concerns the anomalous behaviour of the Joukowski optimum rotor at very low tip-speed ratio (Fig. 2b). This model results in a power coefficient greater than the Betz limit and tends to infinity for $\lambda \leq 1$. Some authors argued that it is possible in theory to exceed the Betz limit^{28–30} but others affirmed that the condition of a constant circulation results in a nonphysical solution at small tip-speed ratios.^{24,27,31} Sørensen in § 6 in Ref. 27 summarised the theoretical and computational works on the Joukowski model and concluded by emphasising the need for further experimental investigation.

Having identified the controversy of the general momentum theory at low-tip speed ratio, the next section of this paper focuses on the design of turbines with the three different optimum induction factors distributions presented herein.

III. DESIGN OF THE TURBINES

The expressions for the chord length and pitch angle distribution for all three optimum rotors are obtained by applying the Blade Element/Momentum Theory.

The local torque $d\tau$ acting on a blade element can be obtained either by using the general momentum theory (Eq. 8) or by adopting a blade element approach. Considering a rotor element, the local torque is calculated by projecting the local lift force on the rotor plane (see Fig. 1):

$$d\tau = 1/2 \rho c N W^2 C_l \sin(\varphi) r dr \quad (13)$$

where φ is the angle between the relative velocity W and the

rotor plane:

$$W = \sqrt{C_z^2 + (C_\theta + U)^2} \quad (14)$$

$$= V_\infty \sqrt{(1-a)^2 + \lambda^2 x^2 (1+a')^2} \quad (15)$$

Tip-losses effects and drag were not taken into account in the local torque. Then, combining Eqs. 8 & 13 results in the following expression for the local blade solidity σ :

$$\sigma = \frac{4\lambda x^2 a'}{C_l \sqrt{(1-a)^2 + \lambda^2 x^2 (1+a')^2}} \quad (16)$$

where $x = r/R_T$. The spanwise chord length distribution is then calculated according to Eq. 2. The local pitch angle β is obtained according to the velocity triangle (Fig. 1):

$$\beta = \varphi - \alpha_O \quad (17)$$

where α_O is the optimum angle of attack of the selected airfoil, *i.e.* the angle which gives the best lift to drag ratio and φ is the relative angle. The relative angle is obtained with the help of the flow velocity distributions in the rotor plane:

$$\tan(\varphi) = \frac{(1-a)}{\lambda x(1+a')} \quad (18)$$

In the current study, all three turbines have $N = 8$ blades, a tip radius $R_T = 100$ mm, a hub ratio $H = 0.3$ and a design tip-speed ratio $\lambda = 1$. SG6042 airfoil was selected for the rotors blades because of the high lift-to-drag performance at low Reynolds number and the availability of experimental data in low Reynolds number conditions.^{32,33} 2D airfoil polar plots at Reynolds number $Re = 10^5$ were digitised from the experimental database of Selig *et al.*³² to collect the optimum angle of attack and the lift and drag coefficients, required in the design method.

Turbine's local pitch angle β and blade solidity σ were computed according to Eqs. 16&17. The optimum rotors of Glauert, Betz and Joukowsky were designed with their respective optimal distribution of induction factors at $\lambda = 1$ (Tab. I and Fig. 2a) and with a constant angle of attack along the span $\alpha_O = 6^\circ$. The resulting blade solidity and pitch angle distributions for all three rotors can be seen in Fig. 3. All turbines' design specifications are reported in Tab. II.

The rotors were drawn in FREECAD and printed by Fused Material Deposition (FMD) on a Creality CR-10 Max printer. PLA (Polylactic Acid) was selected for use with the 3D printed wind turbines developed herein. The printing time and filament mass required are detailed in Tab. II and the Fig. 4 shows the 3D CAD of all three rotors. A specific marker, displayed in the last row of Tab. II, is assigned for each optimum runner.

IV. EXPERIMENTAL SETUP

Wind tunnel experiments play an essential role in the optimisation of wind turbine design. The present experiments serve two purposes: firstly, to determine the performance characteristics of the three turbines depicted in the previous

TABLE II: **Wind turbines specifications.** The length refers to the length of the hub. See Tab. I and Fig. 2 for Glauert's and Joukowsky's optimal induction factors distributions

	Betz	Glauert	Joukowsky
R_T [mm]	100	100	100
H [mm]	0.3	0.3	0.3
λ	1.0	1.0	1.0
Airfoil	SG6042	SG6042	SG6042
α_O [deg]	6	6	6
a	1/3	Glauert	Joukowsky
a'	0	Glauert	Joukowsky
$C_{p,max}$	0.593	0.397	0.572
$\sigma(R_H)$	3.93	1.38	2.53
$\sigma(R_T)$	0.74	0.54	0.69
$\beta(R_H)$ [deg]	60	43	25
$\beta(R_T)$ [deg]	28	24	22
Volume [cm ⁻³]	416	161	245
Length [mm]	88.7	42.5	42.5
Printing time [h]	42	24	36
Filament mass [g]	304	182	278
Marker	■	+	×

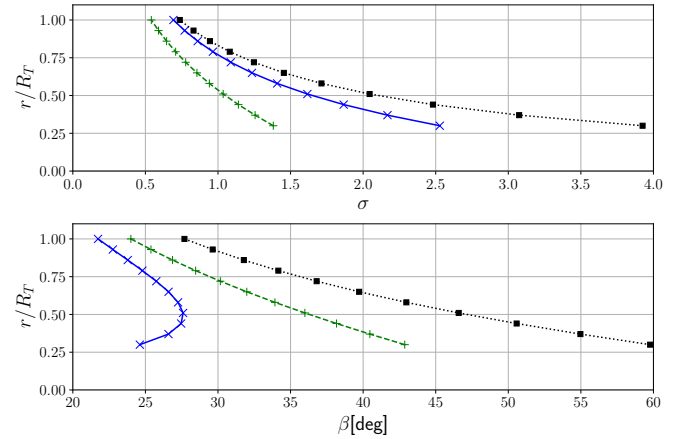


FIG. 3: **Wind turbines blade geometry.** Spanwise variations of the local blade solidity σ (up) and pitch angle β (down) for the optimum rotor of Betz (■), Glauert (+) and Joukowsky (×)

section, and secondly, to investigate the flow velocity distributions upstream and downstream the turbines for three operating tip-speed ratio. The experimental data collected in this study could also provide key insights to develop reliable numerical models.²⁷

The experimental campaign was performed in the closed circuit wind tunnel of the LIFSE facilities.³⁴ The test section size of this wind tunnel is 1.35 m (height) \times 1.65 m (width) \times 1.80 m (length). Regarding the dimension of the turbine models tested, the effect of wind tunnel blockage ratio ($\leq 1.5\%$) on the wake development can be reasonably neglected.

One aim of the current experimental study is to determine the full C_p vs. λ and C_τ vs. λ curves for all three rotors, hence an experimental setup was specifically designed to achieve

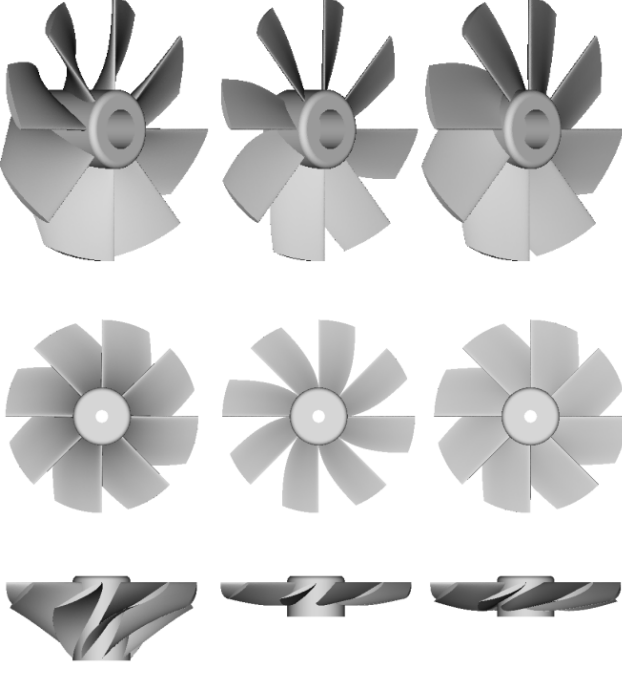


FIG. 4: **Solid models** of the optimum rotors of Betz (left), Glauert (middle) and Joukowsky (right)

this purpose. All the experiments were performed at a fixed flow velocity in the test chamber $V_\infty = 15 \text{ m.s}^{-1}$. The undisturbed wind speed was measured *via* a Pitot probe placed in the test section and was corrected with the daily air density. The variation of the tip-speed ratio was therefore executed by changing the angular velocity of the rotor. During an acquisition, the turbine model was mounted on a rotating shaft located in the middle of the test section. An electric MAXON DC motor and a rotating torquemeter HBM T20 WN, were coupled to the turbine's shaft. The latter were housed in a nacelle. The motor was connected to a variable resistor and was working as generator. The angular velocity of the rotor was maintained constant during a sample. Both angular velocity and torque were measured by the torque transducer while the electric motor enabled to vary the angular velocity of the turbine *i.e.* the operating tip-speed between each sample by changing the electrical load. For each sample, the average torque, angular velocity and wind speed were computed from 50 s recordings with a sampling frequency of 1000 Hz. Then, average torque coefficient C_τ and power coefficient C_p were calculated for each tip-speed ratio according to Eq. 9 and Eq. 10. This experimental procedure was repeated several times on different days for all three rotors. The data were finally gathered and plotted on graphs showing the variation of C_p and C_τ with the tip-speed ratio λ (displayed in § V).

The second objective is to investigate the airflow velocity fields upstream and downstream the wind turbines. Thus, phase-averaged and phase-locked three components stereoscopic particle image velocimetry (SPIV) were performed with the turbines operating at $V_\infty = 15 \text{ m.s}^{-1}$ and for three tip-speed ratio $\lambda = 0.5 - 1 - 1.4$. A sketch of the experi-

mental set-up with the SPIV velocity measurement plane is displayed in Fig. 5. Mathematical, theoretical and technical backgrounds of three-components SPIV techniques can be found in Ref. 35.

During an acquisition, both angular velocity *i.e.* tip-speed ratio and wind speed were kept constant. The wind tunnel was continuously seeded with micro oil droplets generated by an oil mist generator 10F03 Dantec. The oil tracers were illuminated twice within a $90 \mu\text{s}$ time interval by a double pulsed Nd-Yag Litron Nano-L 200-15 laser. The laser was placed above the test section and settled to align the laser sheet with the turbine's rotation plane. The SPIV images were acquired by two 2048×2048 pixels CCD cameras equipped with Micro-Nikkor AF60 mm f/2.8D lenses and Scheimpflug system to enhance image quality. On one hand, laser and cameras were triggered at the same azimuthal position of the blade to obtain 200 double frame phase-locked images. On the other hand, 500 phase-averaged images were collected by triggering the laser and the cameras with an internal clock set at 2 Hz. Prior to data recording, the calibration procedure of the two cameras was carried on with a $200 \text{ mm} \times 200 \text{ mm}$ calibration target. The pinhole camera model, proposed by Dantec, was then used to determine the calibration matrix of the two cameras.

After data recording, SPIV images were processed using Dynamic studio v4.15 software. The images were dewarped and corrected for residual misalignment with the calibration matrix. Then, they were divided into 32×32 pixels interrogation windows where the axial C_z , tangential C_θ and radial C_r velocity vectors were reconstructed using a cross-correlation algorithm. The dimensionless velocity fields were calculated from the 500 phase-averaged images and 200 phase-locked images for all three turbines and tip-speed ratios and normalised with the freestream wind velocity V_∞ collected from the Pitot probe. Finally, the dimensionless phase-averaged and phase-locked vorticity fields $\omega_y R_T / V_\infty$ were calculated according to:

$$\omega_y \frac{R_T}{V_\infty} = \left(\frac{\partial C_r}{\partial z} - \frac{\partial C_z}{\partial r} \right) \frac{R_T}{V_\infty} \quad (19)$$

where ω_y is the out-of-plane vorticity. In the current study, the initial wake expansion downstream the turbines was characterised by the locations of the tip-vortex cores, collected from phase-locked vorticity fields.^{36,37} The reference frame origin for the analysis and comparison of the dimensionless velocity and vorticity fields and profiles is located at the intersection of the blade leading edge with the rotation axis.

V. RESULTS AND DISCUSSION

A. Performance analysis

Fig. 6 shows the variations of the torque coefficient C_τ and power coefficient C_p with the tip-speed ratio and Tab. III highlights the major characteristics of all three runners. The power characteristics are discussed in the following section § V A 1 and the starting behaviour is examined in § V A 2.

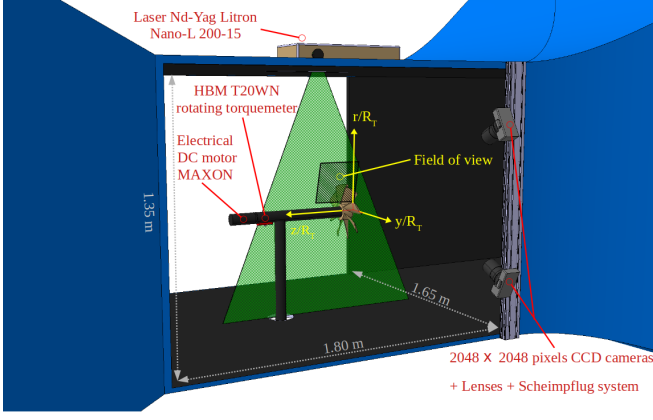


FIG. 5: Sketch of the experimental set-up

1. $C_p - \lambda$ and $C_\tau - \lambda$ curves

Fig. 6b and Tab. III show that the Glauert optimum rotor achieves higher maximum power coefficient ($C_{p,max} = 0.34$) than the optimum rotors of Betz ($C_{p,max} = 0.31$) and Joukowski ($C_{p,max} = 0.26$). Glauert (+) and Joukowski (x) rotors reach their maximum efficiency at the tip-speed ratio $\lambda_{opt} = 1.4$ whereas the optimum rotor of Betz (■) achieves it at the design tip-speed ratio $\lambda_{opt} = 1$. All three rotors' maximum power coefficients are significantly lower than the theoretical one (Tab. II) and the slightest relative difference is observed with the optimum rotor of Glauert (14%). Even though the rotor designed according to the optimum flow conditions of Joukowski theoretically results in performance that can exceed the Betz limit, the experiments carried out in this study highlight the significant relative difference between theoretical and experimental maximum power coefficients (55%). The analysis of the flow velocity distributions carried out in the § VB will provide a greater understanding of this discrepancy. At low tip-speed ratio, for $0 \leq \lambda \leq 0.9$, the optimum rotor of Betz achieves higher power coefficient than the two other runners but its performance strongly decreases for $\lambda \geq 1.6$.

For the analysis of C_τ vs. λ curves, Fig. 6a will be read from right to left *i.e.* from high tip-speed ratio to low tip-speed ratio. As shown in Fig. 6a, the torque coefficient of the optimum rotors of Betz (■) and Joukowski (x) increases linearly when the tip-speed ratio decreases for the entire operating range. This peculiarity is helpful for the power management of IoT devices, especially if the turbine can operate in a wide range of C_τ . It allows a sensitive control of the turbine's angular velocity with a resisting torque control strategy and ensures the powering of a battery at constant voltage.³⁸ On the contrary, non linear variations of C_τ with the tip-speed ratio are observed with the optimum rotor of Glauert (+). From $\lambda = 2.3$ to $\lambda = 0.75$ the torque coefficient increases quasi-linearly with the tip-speed ratio. Then, after remaining constant for $0.75 \geq \lambda \geq 0.5$, the torque coefficient increases again to $C_\tau = 0.4$ at $\lambda = 0.25$ and finally drops to $C_{\tau 0} = 0.33$ at $\lambda = 0$.

C_τ vs. λ variations are closely related to the wind turbine blade geometry and the airfoil aerodynamic characteristics. Experimental lift and drag polar plots of the SG6042 airfoil collected in wind tunnel with a single airfoil show that the lift coefficient increases with the angle of attack until a critical angle called the stall angle $\alpha_c \approx 13^\circ$.³² As C_l increases with the angle of attack before the stall, so does the torque coefficient of all three turbines when the tip-speed ratio decreases (read Fig. 6a from right to left). For an isolated airfoil, the flow starts to separate on the upper surface at the stall angle α_c due to a high pressure gradient between the suction and the pressure sides. The detachment of the boundary layer leads to a significant drop of the lift coefficient. The variations of the aerodynamic coefficients with the angle of attack in post-stall region *i.e.* for $\alpha \geq \alpha_c$ has received scant attention in the research literature, hence the understanding of wind turbine's behaviour for $\lambda \leq \lambda_{opt}$ is hampered by a lack of experimental data. Nevertheless, the available experimental high angle of attacks polar plots collected by Kostic *et al.*³⁹ with NACA airfoils provide some relevant insights to analyse wind turbine's behaviour in post-stall region. Data from this paper show that C_l remains quasi-constant after the stall and then increases for angles of attack from $\alpha = 30^\circ$ and $\alpha = 65^\circ$. Above $\alpha = 65^\circ$, C_l decreases with the angle of attack. On the opposite, even though in pre-stall region the drag coefficient is low, it increases strongly with α in post-stall region and can exceed the lift coefficient. Consequently, for tip-speed ratio much lower than the optimum tip-speed ratio, the drag force contributes significantly to the aerodynamic torque produced by a wind turbine especially if the latter has a large blade solidity. It emphasises that from $\lambda = 0$ to λ_{opt} , high solidity micro-scale turbines change from drag-type to lift-type turbines and this might partially explain why no drop of C_τ are observed.

C_τ vs. λ curves of low blade solidity wind turbines ($\sigma \leq 0.5$) have similar pattern of variation than C_l vs. α curves of isolated airfoils because the blades are sufficiently distant from each other. However, a decrease in blade spacing can lead to mutual interactions between pressure and suction sides of two adjacent blades affecting the airfoil characteristics (stall angle, lift and drag coefficients) and the wind turbine's behaviour (optimum tip-speed ratio, torque and power coefficients).⁴⁰ The change in the shape of C_τ vs. λ curves between the two high-solidity runners of Betz and Joukowski and the runner of Glauert, which have a lower solidity, underlines this blade interference effect. Indeed, C_τ vs. λ curve of the Glauert's optimum rotor have a quite similar pattern of variation of C_l vs. α curves, even if this rotor has a larger solidity than conventional rotor, whereas no significant stall effects are observable on C_τ vs. λ curves of Betz' and Joukowski's optimum rotor.

These findings suggest that high solidity wind turbines should not be considered as a sum of individual airfoils but as a blade cascade arrangement. It also outlines some limitations of the blade element momentum theory for the design of high-solidity micro-scale wind turbines. The assumption of independent operation of the blades made in the design method seems not to be confirmed by the experimental results. The mutual blade interactions make the validity of the airfoil data

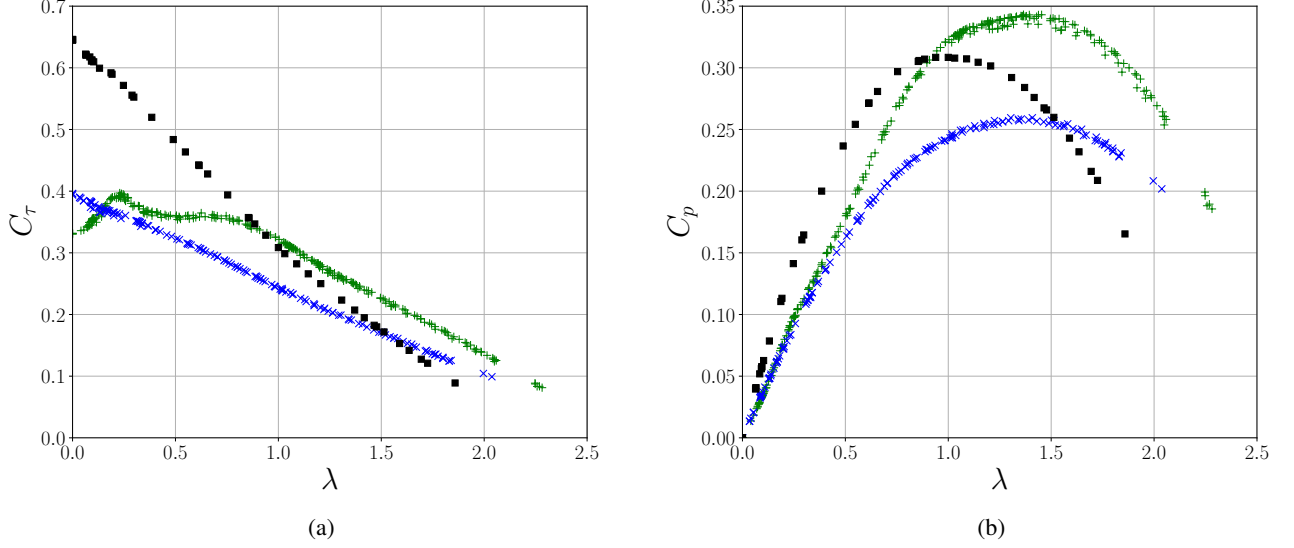


FIG. 6: Torque coefficient C_τ (a) and power coefficient C_p (b) evolution as a function of the tip-speed ratio λ for the optimum rotor of Betz (■), Glauert (+) and Joukowsky (×)

questionable to compute the blade solidity and blade pitch angle whereas accurate data are required in the design method.²⁸ A design methodology based on flow deflection rather than on airfoil polar plots (as it is done for the design of pumps, compressors and turbines in a confined flow) could be of great interest for the design of high-solidity turbine.³⁴ It would help to understand and evaluate the interaction between a blade cascade in rotation and an unconfined airflow. The latter would require investigations on the behaviour of a turbine blade cascade through the collection of the aerodynamic coefficients of an airfoil settled inside a blade cascade as some experience have already been performed with compressor cascade.^{41,42}

Finally, understanding of C_τ vs. λ and C_p vs. λ curves requires a precise knowledge on the flow pattern upstream and downstream the runners for their entire range of tip-speed ratio. As an explanation based on airfoil polar plots remains limited, the analysis provided in § V B is based on the flow velocity fields computed from SPIV recordings with the turbines running at different tip-speed ratios.

2. Starting behaviour

As micro-scale wind turbines should operate mainly within a urban environment, where the average wind speed is low, it is crucial to have runners with very low cut-in wind speed to commence power extraction in low wind speed conditions. Like the operation at low tip-speed ratio, the starting behaviour of micro-scale wind turbines is a challenging subject because it deals with several complex aerodynamic phenomena such as unsteadiness, high angles of attack and very low Reynolds numbers.^{43,44} Despite the importance of this subject, only few published studies have closely exam-

ined wind turbine starting behaviour. Consequently, very few turbines are specifically designed to achieve a low cut-in wind speed. In the current study, the initial torque coefficient $C_{\tau 0} = C_\tau(\lambda = 0)$ and the cut-in wind speed V_0 are used to evaluate the starting behaviour of all three optimum runners.

As shown in Fig. 6a and Tab. III, the optimum rotor of Betz produces higher initial torque coefficient than the rotors of Joukowsky and Glauert. The cut-in wind speed measures reveal also that the Betz rotor is able to harvest the energy of lower airflow speeds (Tab. III).

Like most micro-scale wind turbines, all three rotors are fixed pitch turbines, hence they require high lift blades to increase the starting torque.⁴⁵ The total lift force acting on a blade element depends on the blade section airfoil, the chord length and the angle of attack. As an increase in the chord length increases the lift force acting on an airfoil so does the torque coefficient of a wind turbine with an increase in the blade solidity.⁴⁰ It partially explains why the Betz and Joukowsky rotors have larger $C_{\tau 0}$ and lower V_0 than the rotor of Glauert. However, the results show little difference in $C_{\tau 0}$ between the runners of Glauert and Joukowsky whereas the latter has a much larger blade solidity. This can be explained by the difference in the angle of attack between rotors. As the turbines are not rotating at $\lambda = 0$, the flow relative angle tends to $\varphi = \pi/2$, hence the angles of attack are high and the flow over the airfoil is detached. In post-stall region, larger blade pitch angles *i.e.* lower angles of attack lead to higher lift forces.³⁹ Consequently, even though, the optimum rotor of Joukowsky has larger blade solidity than the Glauert rotor, the higher angles of attack reached in the post-stall region with the Joukowsky rotor may lead to a decrease in the lift force reducing the starting torque coefficient.^{46,47}

As experimental polar plots of the SG6042 airfoils are not

TABLE III: Optimum rotor's major characteristics computed from torque transducer acquisitions

	Betz	Glauert	Joukowski
$C_{p,max}$	0.31	0.34	0.26
λ_{opt}	1.0	1.4	1.4
V_0 [m.s ⁻¹]	3.7	5.1	4.6
$C_{\tau 0}$	0.65	0.33	0.39

TABLE IV: Power coefficient C_p computed from SPIV recordings

	$\lambda = 0.5$	$\lambda = 1$	$\lambda = 1.4$
Betz	0.22	0.31	0.30
Glauert	0.18	0.30	0.34
Joukowski	0.13	0.21	0.21

available for high angles of attack in post-stall region, further research on the flow velocity downstream the rotors at $\lambda = 0$ should be conducted to provide relevant information on the starting behaviour of a micro-scale wind turbine. This study could be supported by an experimental investigation of the aerodynamic properties of isolated airfoils and blade cascade in post-stall region and in low Reynolds number flow conditions.

B. Near wake analysis

As concluded in the previous section, the power characteristics reveal the global performance of all three turbines but a full investigation of the airflow upstream and downstream all three runner provides a better understanding of the interaction between the airflow and the turbines and on the science of generating torque from wind energy.

Velocity fields - Profiles

Fig. 7 and Fig. 8 show the phase-averaged dimensionless axial and tangential velocity fields in the wake of the wind turbine models for three tip-speed ratios $\lambda = 0.5$, $\lambda = 1$ and $\lambda = 1.4$.

For all optimum runners, a decrease in the operating tip-speed ratio leads to lower axial velocity and larger tangential velocity of the wake airflow, especially near the turbine nacelle. A large recirculation region was found in the wake of the optimum rotors of Joukowski and Glauert. Even though the size of the recirculation region decreases for both turbines with the tip-speed ratio and almost disappears for the Glauert's optimum rotor at $\lambda = 1.4$, this region extends over almost half of the blades and for the entire near wake of the optimum rotor of Joukowski. The decrease in the size of the recirculation region is in agreement with the increase of the power coefficient, computed either from the velocity fields (Tab. IV) or from the torque transducer (Tab. III), when the tip-speed ra-

tio increases from $\lambda = 0.5$ to $\lambda = 1.4$. No recirculation region are noticed downstream the optimum rotor of Betz. The wake downstream the optimum rotor of Betz is more stable and shows larger tangential velocity than the two other runners. The radial profiles of the phase-averaged normalised axial and tangential velocities for various horizontal distance from the blade leading edge, displayed in the supplementary materials, highlight the stability and the persistency of the wake downstream the optimum rotor of Betz. This turbine could be of particular interest in association with a rear counter-rotating turbine harvesting the highly rotating airflow in its wake. Moreover, the radial profiles point out the back-flow downstream the optimum rotor of Glauert ($C_z/V_\infty \approx -0.2$ for $\lambda = 0.5$ and at $(r/R_T, z/R_T) = (0.3, 3/2)$) and downstream the optimum rotor of Joukowski ($C_z/V_\infty \approx -0.3$ for $\lambda = 0.5$ and at $(0.3, 3/2)$).

Fig. 9 shows the radial variations of the axial induction factor a (1st row), tangential induction factor a' (2nd row), angle of attack α (3rd row) and infinitesimal torque coefficient dC_τ (4th row) for all three tip-speed ratios and optimum rotors. These experimental data were calculated with the velocity fields collected from the SPIV recordings and according to the equations introduced in § II. a , a' and α profiles were computed just upstream the optimum rotors of Glauert and Joukowski, at $z/R_T = -0.02$ (semi-transparent lines) and a , a' and dC_τ downstream all three rotors at $z/R_T = 3/4$ (full lines). The region upstream the optimum rotor of Betz was outside of camera range, hence neither the induction factors nor the angle of attack were measured. Black crosses (+) represent design parameters (Tab. II).

Firstly, Fig. 9 emphasises the effects of the tip-speed ratio on the airflow characteristics. For all three turbines, an increase in the tip-speed ratio leads to lower axial and tangential induction factors and a decrease in the infinitesimal torque coefficient, which corroborates the observation of the velocity fields and the pattern of variation of C_τ vs. λ curves. Moreover, the angle of attack profiles of the optimum rotor of Glauert and Joukowski show that the inflow angle of attack α is closer to the design optimum angle of attack α_0 at $\lambda = 1.4$ than at the design tip-speed ratio $\lambda = 1$. It explains why both runners achieve their maximum power coefficient at $\lambda = 1.4$. From the α profiles, it is also apparent that the angle of attack varies along the span of the blades even though the angle of attack was set constant in the design method. The main discrepancies are observed near the root of the blades where the flow is strongly affected by the rotor's hub and the nacelle. As the angle of attack are too large in the lower part of the blades, a possible improvement would be to increase the geometric blade pitch angle in the design. What is interesting is that, even though all three turbines are designed to achieve their maximum efficiency at $\lambda = 1$, the runner designed with the most basic aerodynamic model, the Betz optimum flow conditions, is the only one that reaches its maximum performance at the desired tip-speed ratio.

Secondly, closer examination of the airflow characteristics at the design tip-speed ratio $\lambda = 1$ reveals interesting findings. Even though the assumptions of a constant axial induction factor $a = 1/3$ and no rotational velocity made in the design of

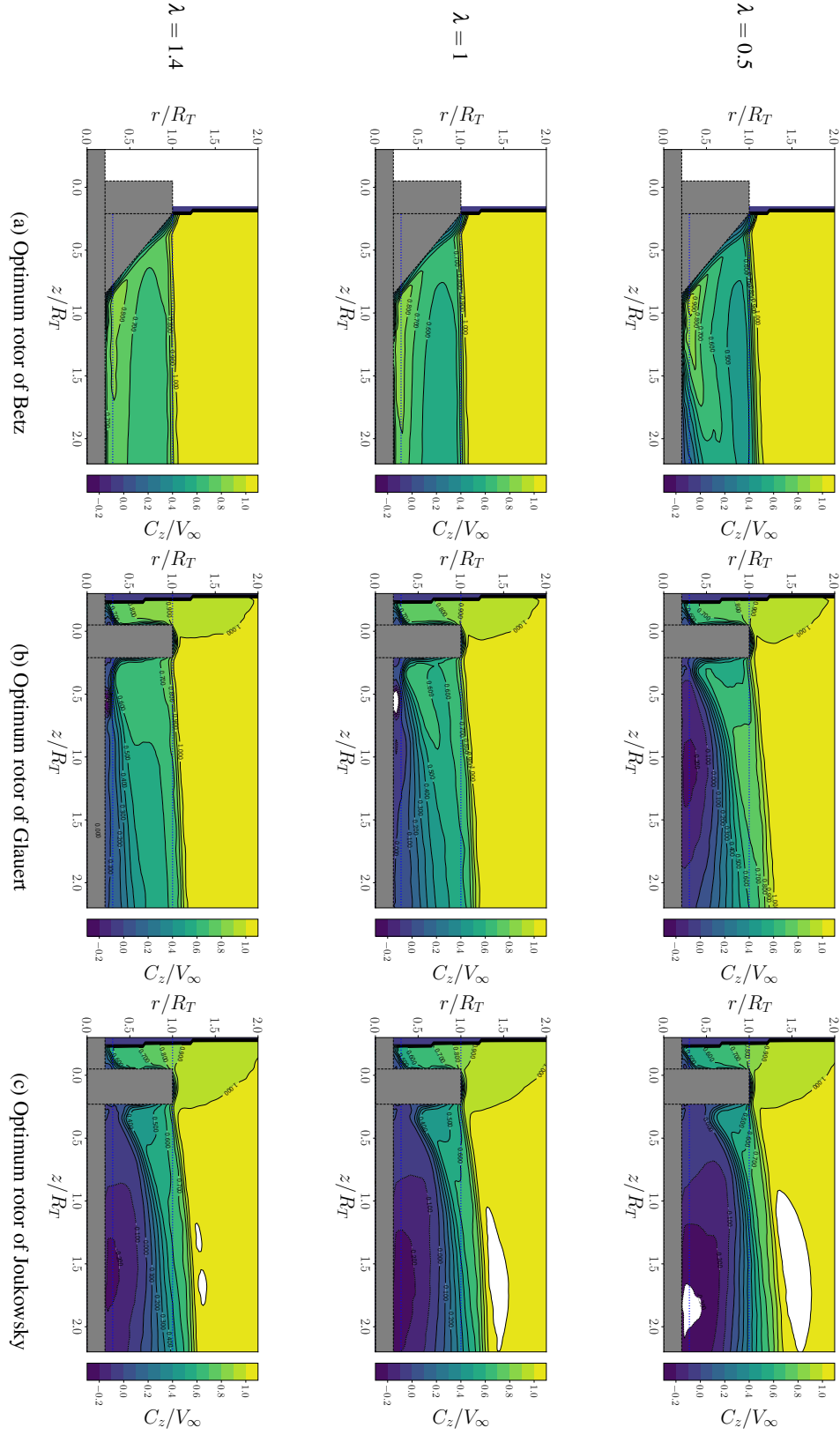


FIG. 7: **Phase-averaged dimensionless axial velocity fields** C_z/V_∞ collected from SPIV acquisitions with the optimum rotor of Betz (a), the optimum rotor of Glauert (b) and the optimum rotor of Joukowski (c) operating at $\lambda = 0.5$ (1st row), $\lambda = 1$ (2nd row) and $\lambda = 1.4$ (3rd row).

the optimum rotor of Betz are not verified experimentally, this runner still achieves a good power coefficient and at its design

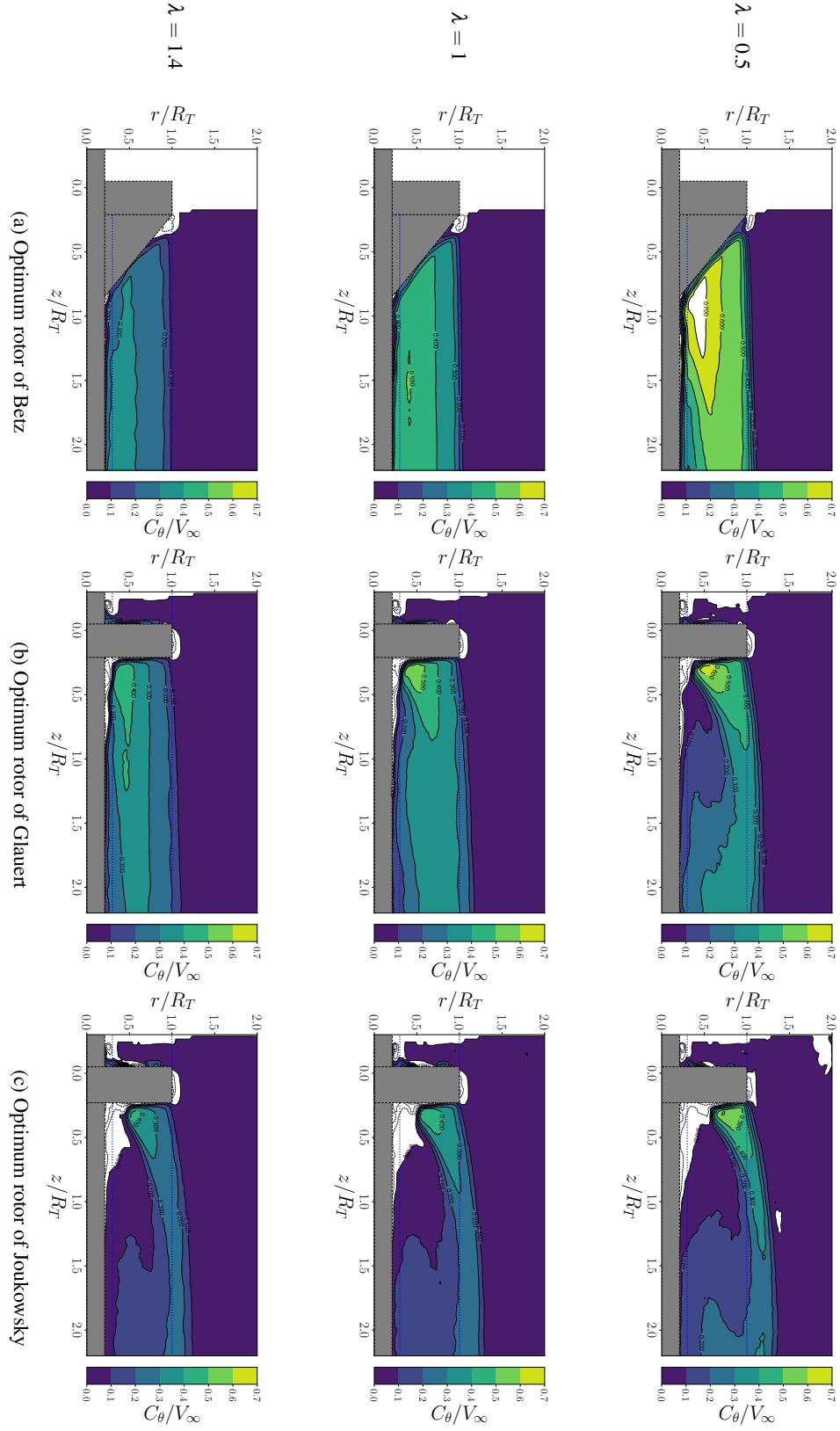


FIG. 8: **Phase-averaged dimensionless tangential velocity fields** C_θ/V_∞ collected from SPIV acquisitions with the optimum rotor of Betz (a), the optimum rotor of Glauert (b) and the optimum rotor of Joukowski (c) operating at $\lambda = 0.5$ (1st row), $\lambda = 1$ (2nd row) and $\lambda = 1.4$ (3rd row).

tip-speed ratio. For the optimum rotor of Glauert, the tangential induction factor immediately behind the rotor plane is

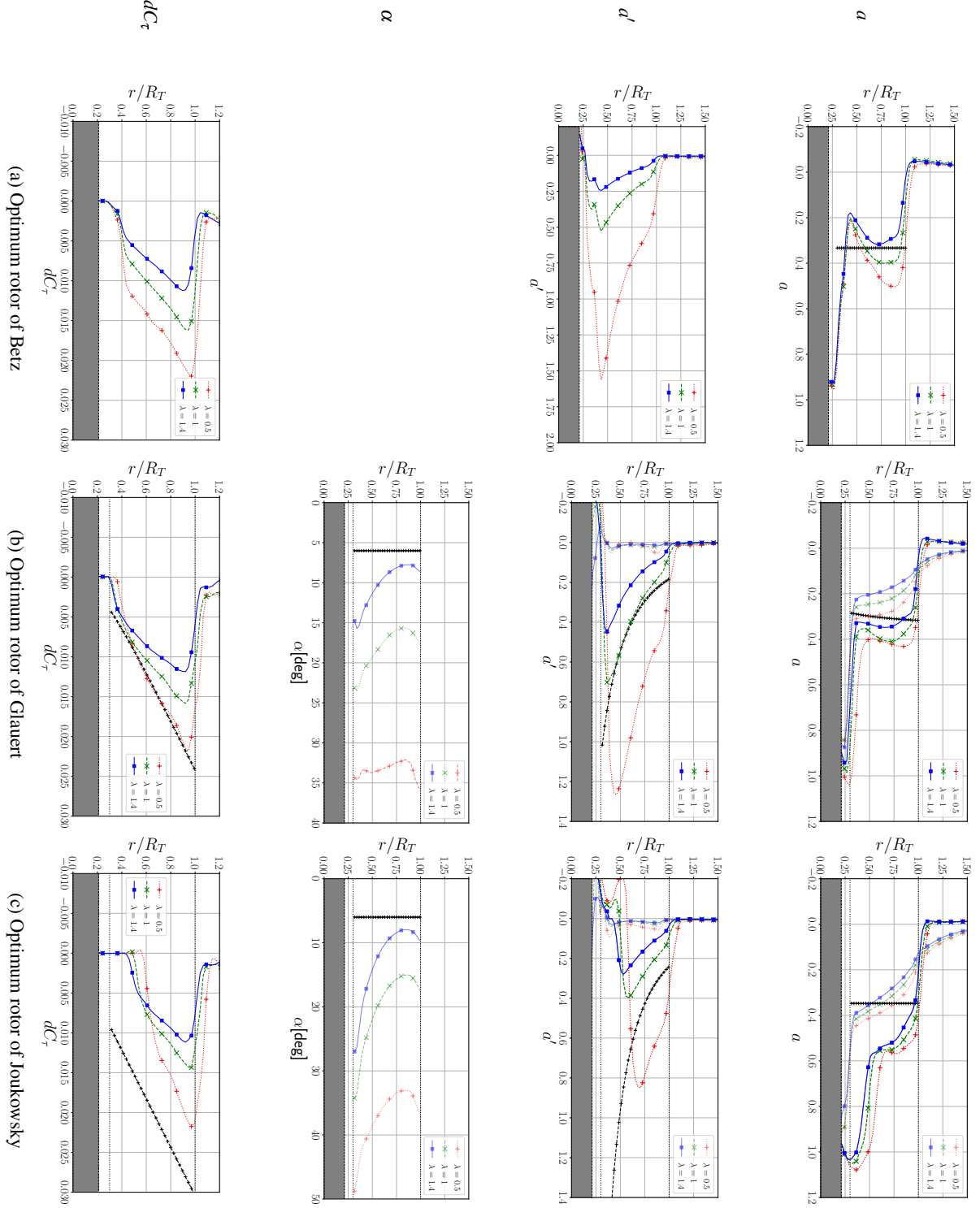


FIG. 9: **Induction factor, angle of attack and torque coefficient loading spanwise variations** collected from SPIV acquisitions with the optimum rotor of Betz (a), the optimum rotor of Glauert (b) and the optimum rotor of Joukowsky (c) for three tip-speed ratios. These parameters are computed at $z/R_T = 3/4$ (full lines) and $z/R_T = -0.02$ (semi-transparent lines). Black crosses (+) represent the design parameters at $\lambda = 1$.

very close to the design setting. Some discrepancies are ob-

served between the axial induction factor just downstream the

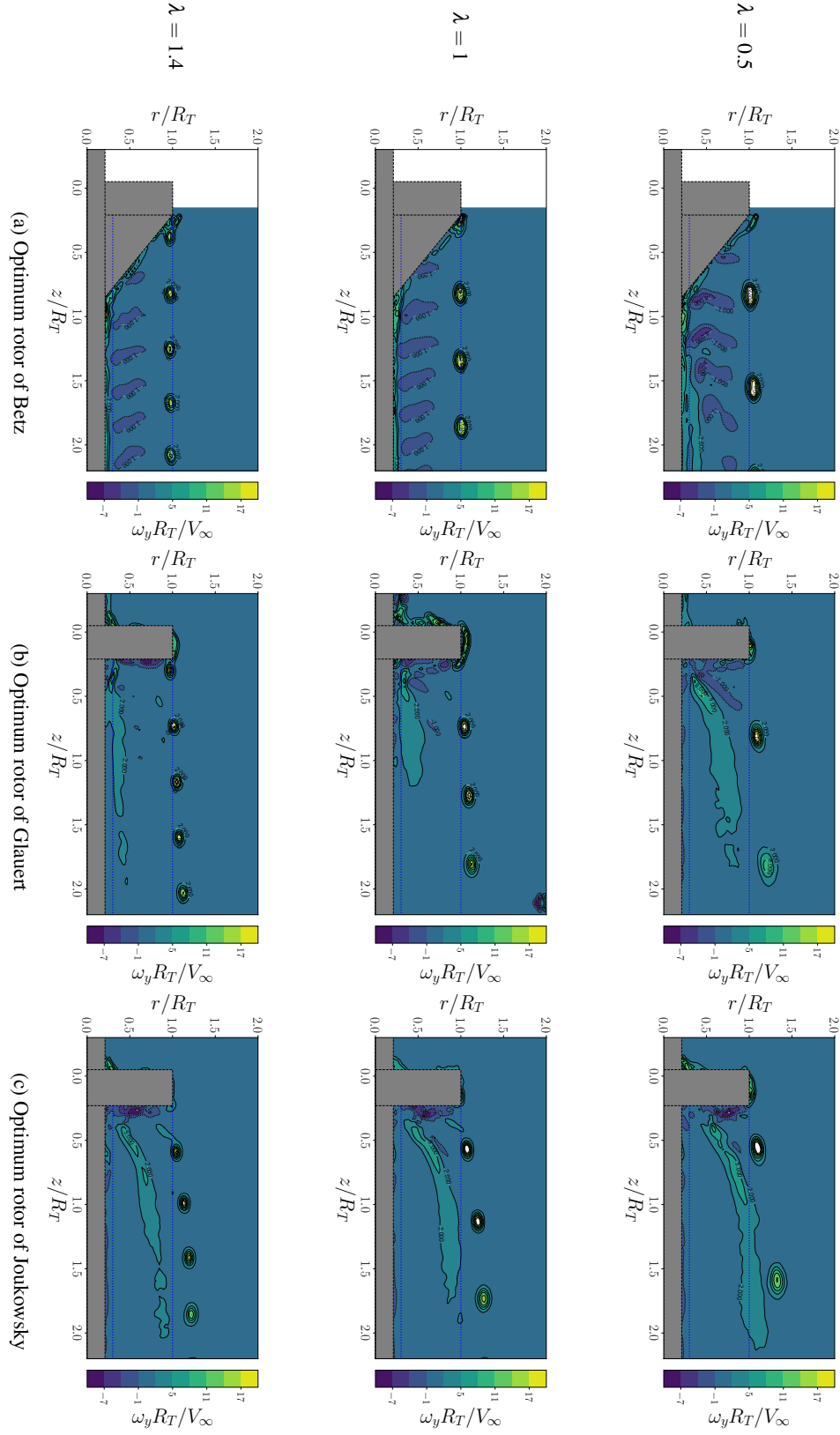


FIG. 10: **Phase-locked dimensionless vorticity fields** $\omega_y R_T / V_\infty$ collected from SPIV acquisitions with the optimum rotor of Betz (a), the optimum rotor of Glauert (b) and the optimum rotor of Joukowski (c) operating at $\lambda = 0.5$ (1st row), $\lambda = 1$ (2nd row) and $\lambda = 1.4$ (3rd row).

rotor and the design setting. However, the latter is close to the average between a immediately upstream (transparent lines)

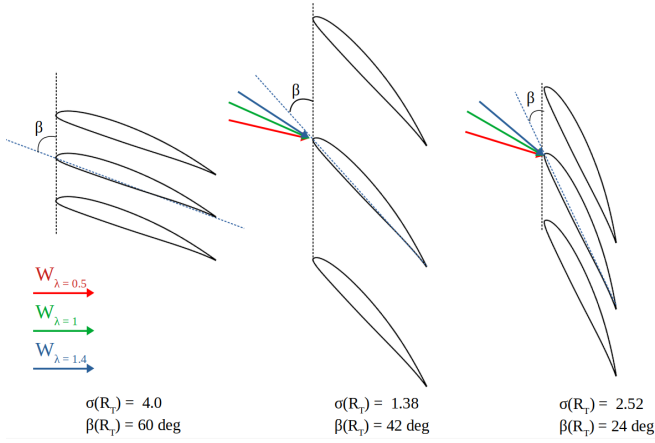


FIG. 11: Graphic illustration of flow deflection and blockage effect. Sketch of the blade cascade arrangement at $r = R_H$ for the optimum rotor of Betz (left) Glauert (middle) and Joukowski (right). Relative velocity vector orientations are calculated from the SPIV recordings for all three tip-speed ratios

and downstream (full lines) the rotor. All models are based on the actuator disk theory, hence the definition of a in the rotor plane is controversial because it doesn't take into account the physical aspect of the blade. Finally, high differences between the design settings and the experimental data are observed with the Joukowski rotor. For all tip-speed ratio, $a \leq 1$ near the nacelle which highlights large recirculation area. The assumption of a rotor disc with a constant circulation seems inappropriate for low tip-speed ratio wind turbines.

The recirculation region, near the hub of the Glauert and Joukowski rotor could be attributed to the significant flow deflection imposed by both turbines. A sketch of the blade cascade arrangement at the particular radius $r = R_H$ is displayed in Fig. 11 to provide a better understanding of the fluid blockage effects. For all three rotors and tip-speed ratios, the relative velocity vector W is drawn in accordance with the angle of attack measured at $r = R_H$. As shown in this figure, even though the blade solidity of the optimum rotor of Betz is higher than the blade solidity of the two other runners, the larger deflection imposed by the Joukowski and Glauert rotors leads to larger flow obstruction, especially at low tip-speed ratio. Lower pitch angle distribution induces larger angle of attacks at $\lambda = 0.5$ and therefore separation of the flow. In addition, a turbine geometry that obstructs too much the fluid, due to an appropriate combination of blade solidity and pitch angle distribution, leads to recirculation bubbles, vortex breakdown and a drop in performance. All these physical phenomena are not taken into account in the general momentum theory because there is first no consideration of the physical behaviour of the blade and secondly because the flow is assumed inviscid. Even though, the angle of attack along the blade of the optimum rotor of Betz was not measured in the study, it can be suggested that the flow does not separate at $\lambda = 0.5$ due to larger pitch angle distribution.

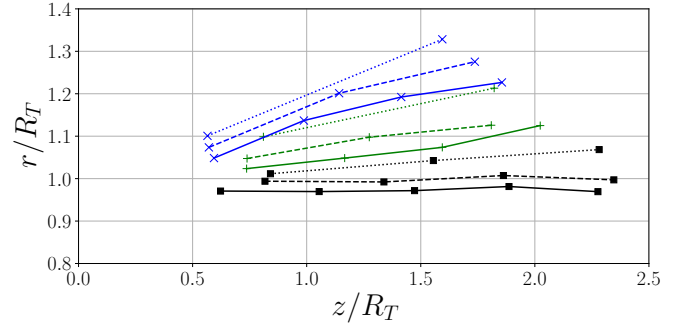


FIG. 12: Initial wake expansion. Locations of the vortex cores downstream the optimum rotor of Betz (■), Glauert (+) and Joukowski (×) collected from phase-locked SPIV vorticity fields (Fig. 10). The wind turbines were operating at $\lambda = 0.5$ (····), $\lambda = 1$ (---) and $\lambda = 1.4$ (—).

Vorticity and wake expansion

Fig. 10 shows the phase-locked normalised out of plane vorticity fields downstream the turbine models, computed according to Eq. 19 with the phase-locked velocity fields. Phase-averaged vorticity fields are displayed in the supplementary materials. As can be observed, a series of tip-vortices is shed downstream the turbines. Moreover, both phase-locked and phase-averaged vorticity fields show two high vorticity regions, in the inner part of the blade and at the tip of the blade.

What stands out in vorticity fields is that for all tip-speed ratio, the intensity of the vorticity near the hub region of the optimum rotor of Betz appeared to be lower than for two other turbines. The vorticity in this region is closely related to the flow separation near the nacelle that leads to a highly turbulent flow. It corroborates the velocity fields showing a large recirculation zone downstream the optimum rotors of Glauert and Joukowski. Moreover, for all three rotors, a decrease in the tip-speed ratio results in higher vorticity intensity in both regions and wider wake expansion. Both strength and vortex core radius decreases as the tip-speed ratio increases.

The locations of the mean vortex core for all three runners and tip-speed ratio are depicted in Fig. 12. As the experiments were performed at fixed wind speed, the number of tip vortices in the investigated area increases with the tip-speed ratio. The lines joining the centre of mean vortex cores have been added to facilitate the visualisation of wake expansion. It can be seen clearly that the wake downstream the optimum rotor of Joukowski is wider than the wake downstream the two other runners for all tip-speed ratios. The wake downstream the optimum rotor of Betz is narrow and persists over long distances behind the runner. As the wind energy in the wake is persistent and remains enclosed in a streamtube with a constant radius, it could be beneficial to collect the remaining energy with an additional runner placed downstream the optimum runner of Betz. The low energy dissipation as well as the low wake expansion allows to place the back rotor far enough away from the front rotor, hence allowing the front one to perform effectively.

VI. CONCLUSION

Recent developments in the field of energy harvesting have aroused new interest in the design of low tip-speed ratio micro-scale wind turbines. The great variety of micro-scale wind turbine's geometry found in the open literature underlines the lack of consensus on the design methodology. This is partly due to the current limitations of the classical design method, the Blade Element/Momentum Theory, at low tip-speed ratio. Depending on the theoretical framework adopted (Betz, Glauert or Joukowsky), the set of equations derived from the general momentum theory differs significantly at low tip-speed ratio, resulting in different blade geometry. The aim of this study was to investigate experimentally the power and airflow characteristics of three 200 mm wind turbines designed according to the optimal flow conditions of Betz, Glauert and Joukowsky at $\lambda = 1$.

Torque and power coefficients vs. tip-speed ratio curves and cut-in wind speeds were obtained by the means of several experiments in the wind tunnel of the LIFSE facilities. Wake expansion and airflow velocity fields upstream and downstream all three turbines were collected using 3D stereoscopic particle image velocimetry (SPIV) techniques for three operating tip-speed ratio.

The optimum runner of Glauert achieves the highest power coefficient $C_{p,max} = 0.34$ but at a tip-speed ratio higher than the design tip-speed ratio $\lambda_{opt} = 1.4$. Even though the runner of Betz was designed with the most basic assumptions, it reaches a good level of performance at the design tip-speed ratio and has a very stable, persistent and narrow wake with no recirculation bubbles and vortex breakdown for its entire range of operation. Moreover, it presents the lowest cut-in wind speed and a wide and linear variation of its torque coefficient with the tip-speed ratio. The experiments carried out with the optimum rotor of Joukowsky reveal significant differences between theoretical and experimental results. The assumption of a flow with a constant circulation results in a high solidity wind turbine with a very low pitch angle distribution. SPIV recordings reveal a severe blockage of the fluid and a large recirculation region in its wake which explain its low efficiency. It emphasises that the theoretical developments derived by Joukowsky and argued by Sharpe²⁸, Lam²⁹ or Wood³⁰ suffer from some limitations to describe the turbine's physical behaviour at low tip-speed ratio. From a power conversion point of view, the Glauert optimum rotor achieves the best performance but it has a higher cut-in wind speed, a non linear variation of its torque coefficient with the tip-speed ratio and a wider wake expansion than the Betz rotor. It could be of particular interest to design an hybrid runner based on the geometry of the optimum rotors of Betz and Glauert.

The current study highlights also the limitations of the Blade Element/Momentum Theory for the design and analysis of low tip-speed ratio micro-scale turbines. Even though the theoretical optimum flow conditions of Glauert are rather close to the experimental results, the reliability of the available airfoil polar plots, required in the blade element method, is highly questionable due to the mutual blade interactions and the low Reynolds numbers flow conditions. Further experi-

ments on the effects of the solidity and the Reynolds number on the aerodynamic properties of an airfoil would provide relevant insights for the design and analysis of high-solidity runners with the classical design method.

Finally, a study of the flow deflection through a fixed blade cascade arrangement should be carried out to fully understand the interaction between an airflow and a high-solidity wind turbine. It would help to derive an alternative design methodology based on flow deflection, as it is done for turbines in confined flow or compressors, rather than on airfoil polar plots.

SUPPLEMENTARY MATERIAL

Please find in the supplementary material

- the velocity fields and profiles
- the axial/tangential induction factors and torque/power coefficient radial distributions in the near wake
- the angle of attack spanwise distributions

for all three turbines and tip-speed ratios collected from SPIV acquisitions.

ACKNOWLEDGMENTS

This research was supported by the French Ministry of Higher Education and Research

DATA AVAILABILITY STATEMENT

The data that support the findings of this study are available from the corresponding author upon reasonable request.

¹Bruno Dorsemayne, Jean-Philippe Gaulier, Jean-Philippe Wary, Nizar Kheir, and Pascal Urien. Internet of things: A definition and taxonomy. 09 2015.

²Andrey Somov and Raffaele Giaffreda. Powering IoT devices: Technologies and opportunities. *IEEE IoT Newsletter*, 2015.

³Quan Wen, Xianming He, Zhuang Lu, Reinhard Streiter, and Thomas Otto. A comprehensive review of miniaturized wind energy harvesters. *Nano Materials Science*, 3(2):170–185, 2021.

⁴Ali M. Eltamaly, Majed A. Alotaibi, Abdulrahman I. Alolah, and Mohamed A. Ahmed. IoT-based hybrid renewable energy system for smart campus. *Sustainability*, 13(15), 2021.

⁵M. Rapin and J-M. Noël. *L'énergie éolienne. Du petit éolien à l'éolien offshore*. Dunod, 2019.

⁶E. Welfonder, R. Neifer, and M. Spanner. Development and experimental identification of dynamic models for wind turbines. *Control Engineering Practice*, 5(1):63–73, 1997.

⁷L. A. Viterna and D. C. Janetzke. Theoretical and experimental power from large horizontal-axis wind turbines. *US Department of energy*, 1982.

⁸D. A. Howey, A. Bansal, and A. S. Holmes. Design and performance of a centimetre-scale shrouded wind turbine for energy harvesting. *Smart Materials and Structures*, 20(8):085021, 2011.

⁹Mohamed Y. Zakaria, Daniel A. Pereira, and Muhammad R. Hajj. Experimental investigation and performance modeling of centimeter-scale micro-wind turbine energy harvesters. *Journal of Wind Engineering and Industrial Aerodynamics*, 147:58–65, 2015.

- ¹⁰Dennis Leung, Y. Deng, and Michael K.H. Leung. Design optimization of a cost-effective micro wind turbine. *WCE 2010 - World Congress on Engineering 2010*, 2:988–993, 2010.
- ¹¹Ravi Anant Kishore and Shashank Priya. Design and experimental verification of a high efficiency small wind energy portable turbine (SWEPT). *Journal of Wind Engineering and Industrial Aerodynamics*, 118:12–19, 2013.
- ¹²Ravi Anant Kishore, Thibaud Coudron, and Shashank Priya. Small-scale wind energy portable turbine (swept). *Journal of Wind Engineering and Industrial Aerodynamics*, 116:21–31, 2013.
- ¹³Ravi Anant Kishore, Anthony Marin, and Shashank Priya. Efficient Direct-Drive Small-Scale Low-Speed Wind Turbine. *Energy Harvesting and Systems*, 1(1-2):27–43, 2014.
- ¹⁴Fabio Mendonca and Joaquim Azevedo. Design and power production of small-scale wind turbines. In *2017 International Conference in Energy and Sustainability in Small Developing Economies (ES2DE)*, pages 1–6, Funchal, Portugal, 2017. IEEE.
- ¹⁵M. Perez, S. Boisseau, P. Gasnier, J. Willemin, M. Geisler, and J. L. Reboud. A cm scale electret-based electrostatic wind turbine for low-speed energy harvesting applications. *Smart Materials and Structures*, 25(4):045015, 2016.
- ¹⁶Ronit K. Singh, M. Rafiuddin Ahmed, Mohammad Asid Zullah, and Young-Ho Lee. Design of a low reynolds number airfoil for small horizontal axis wind turbines. *Renewable Energy*, 42:66–76, 2012. International Symposium on Low Carbon and Renewable Energy Technology 2010 (ISLCT 2010).
- ¹⁷P.D. Clausen and D.H. Wood. Research and development issues for small wind turbines. *Renewable Energy*, 16(1):922–927, 1999.
- ¹⁸Matthew M. Duquette, Jessica Swanson, and Kenneth D. Visser. Solidity and Blade Number Effects on a Fixed Pitch, 50 W Horizontal Axis Wind Turbine. *Wind Engineering*, 27(4):299–316, 2003.
- ¹⁹Abdelgalil Eltayesh, Francesco Castellani, Massimiliano Burlando, Magdy Bassily Hanna, A. S. Huzayyin, Hesham M. El-Batsh, and Matteo Becchetti. Experimental and numerical investigation of the effect of blade number on the aerodynamic performance of a small-scale horizontal axis wind turbine. *Alexandria Engineering Journal*, 60(4):3931–3944, 2021.
- ²⁰Sheng-Huan Wang and Shih-Hsiung Chen. Blade number effect for a ducted wind turbine. *Journal of Mechanical Science and Technology*, 22:1984–1992, 2008.
- ²¹Antonio Brasil Junior, Rafael Mendes, Théo Wirrig, Ricardo Noguera, and Taygoara Oliveira. On the design of propeller hydrokinetic turbines: the effect of the number of blades. *Journal of the Brazilian Society of Mechanical Sciences and Engineering*, 41, 2019.
- ²²David Marten, Julian Peukert, Georgios Pechlivanoglou, Christian Nayeri, and Christian Paschereit. Qblade: An open source tool for design and simulation of horizontal and vertical axis wind turbines. *International Journal of Emerging Technology and Advanced Engineering*, 3:264–269, 03 2013.
- ²³A. Betz. Das maximum der theoretisch möglichen ausnützung des windes durch windmotoren. pages 307–309, 1920. (In German).
- ²⁴H. Glauert. *Airplane Propellers*. Springer Berlin Heidelberg, Berlin, Heidelberg, 1935.
- ²⁵N.E. Joukowsky. *Vortex theory of a rowing screw*. *Trudy Otdeleniya Fizicheskikh Nauk Obshchestva Lubitelei Estestvoznaniya*, volume 16(1). 1912.
- ²⁶M.O.L. Hansen. Aerodynamics of wind turbines: Third edition. *Aerodynamics of Wind Turbines: Third Edition*, pages 1–173, 05 2015.
- ²⁷J.N. Sørensen. *General Momentum Theory for Horizontal Axis Wind Turbines*, volume 4 of *Research Topics in Wind Energy*. Springer International Publishing, Cham, 2016.
- ²⁸D. J. Sharpe. A general momentum theory applied to an energy-extracting actuator disc. *Wind Energy*, 7(3):177–188, 2004.
- ²⁹Gabriel C. K. Lam. Wind energy conversion efficiency limit. *Wind Engineering*, 30(5):431–437, 2006.
- ³⁰D.H. Wood. Including swirl in the actuator disk analysis of wind turbines. *Wind Engineering*, 31(5):317–323, 2007.
- ³¹Jens Nørkær Sørensen and Gijs A. M. van Kuik. General momentum theory for wind turbines at low tip speed ratios. *Wind Energy*, 14(7):821–839, 2011.
- ³²M.S. Selig. *Summary of Low Speed Airfoil Data*. Number vol. 3 in *Summary of Low Speed Airfoil Data*. SoarTech Publications, 1995.
- ³³Pyungho Shin and Keonhoon Kim. Aerodynamic performance prediction of sg6043 airfoil for a horizontal-axis small wind turbine. *Journal of Physics: Conference Series*, 1452:012018, 01 2020.
- ³⁴M. Bourhis, M. Pereira, F. Ravelet, and I. Dobrev. Innovative design method and experimental investigation of a small-scale and very low tip-speed ratio wind turbine. *Experimental Thermal and Fluid Science*, 130:110504, 2022.
- ³⁵M. Raffel, C. Willert, and J. Kompenhans. *Particle Image Velocimetry: A Practical Guide*. Number 3, 2018.
- ³⁶S. McTavish, Daniel Feszty, and F. Nitzsche. Evaluating reynolds number effects in small-scale wind turbine experiments. *Journal of Wind Engineering and Industrial Aerodynamics*, 120:81–90, 09 2013.
- ³⁷R. Soto-Valle, S. Cioni, S. Bartholomay, M. Manolesos, C. N. Nayeri, A. Bianchini, and C. O. Paschereit. Vortex identification methods applied to wind turbine tip vortices. *Wind Energy Science*, 7(2):585–602, 2022.
- ³⁸D.J. Burnham, S. Santoso, and E. Muljadi. Variable rotor-resistance control of wind turbine generators. In *2009 IEEE Power Energy Society General Meeting*, pages 1–6, 2009.
- ³⁹Cedomir Kostic and Bosko Rasuo. Aerodynamic airfoil at critical angles of attack. *Vojnotehnicki glasnik*, 64:784–811, 01 2016.
- ⁴⁰Martin Bourhis, Michael Pereira, and Florent Ravelet. Experimental investigation of the effect of blade solidity on micro-scale and low tip-speed ratio wind turbines. *SSRN*, 2022.
- ⁴¹Satyam Panchal and Vijay Mayavanshi. Experimental study of flow through compressor cascade. *Case Studies in Thermal Engineering*, 10:234–243, 2017.
- ⁴²Robert REY, Ricardo NOGUERA, and Farid BAKIR. Pompes rotodynamiques aérohydrodynamique des profils et aubages de pompes hélices. *Techniques de l'ingénieur Machines hydrauliques, aérodynamiques et thermiques*, base documentaire : TIP151WEB.(ref. article : bm4304), 2013.
- ⁴³P.R. Ebert and D.H. Wood. Observations of the starting behaviour of a small horizontalaxis wind turbine. *Renewable Energy*, 12(3):245–257, 1997.
- ⁴⁴A.K. Wright and D.H. Wood. The starting and low wind speed behaviour of a small horizontal axis wind turbine. *Journal of Wind Engineering and Industrial Aerodynamics*, 92(14):1265–1279, 2004.
- ⁴⁵Joao Henriques, F. Silva, Ana Estanqueiro, and L.M.C Gato. Design of a new urban wind turbine airfoil using a pressure-load inverse method. *Renewable Energy*, 34:2728–2734, 12 2009.
- ⁴⁶M. Shur, P.R. Spalart, M. Strelets, and A. Travin. Detached-eddy simulation of an airfoil at high angle of attack. In W. Rodi and D. Laurence, editors, *Engineering Turbulence Modelling and Experiments 4*, pages 669–678. Elsevier Science Ltd, Oxford, 1999.
- ⁴⁷Seok Ho Lee and Yong Oun Han. Experimental investigation of high-angle-of-attack aerodynamics of low-aspect-ratio rectangular wings configured with naca0012 airfoilsection. *International Journal of Aeronautical and Space Sciences*, 21:303–314, 2020.